J Mater Sci: Mater Electron (2023) 34:344

Effect of argon pressure on the physical characteristics of cadmium telluride (CdTe) thin films by close-spaced sublimation

Afrina Sharmin[1], Syed Shafquat Mahmood[1], Munira Sultana[1], Shahin Aziz[1], Md Aftab Ali Shaikh[1], and Muhammad Shahriar Bashar[1,*]

[1] *Bangladesh Council of Scientific and Industrial Research (BCSIR), Dhaka, Bangladesh*

Received: 6 October 2022
Accepted: 9 November 2022
Published online: 4 February 2023

ABSTRACT

The close-spaced sublimation process (CSS) was used to deposit thin 5.2–6.7 μm CdTe films on the well-scrubbed borosilicate glass in this communication. The pinhole-free CdTe films with good adhesion were produced by adjusting the CSS Ar pressure profile inside the chamber at 250, 500, 750, and 1000 mTorr for 10 min to evaluate the film crystallinity and optoelectronic attributes. The source and substrate temperatures were reserved at 625 °C and 585 °C, respectively, for the deposition of CdTe thin films. Atomic force microscopy (AFM), X-ray diffraction (XRD), scanning electron microscopy (SEM), and a UV–Vis spectrophotometer are employed to investigate the microstructural and optoelectronic properties of these as-deposited films. The polycrystalline CdTe structure was revealed by XRD research, which revealed sharp features peak at (111), (220), and (311) orientations. The grain development relied on the deposition pressure in a SEM investigation. AFM shows mean roughness (Ra) and RMS roughness (Rq) values in the 199–293 nm and 245–357 nm ranges, respectively. The optical band gap ranged between 1.45 and 1.55 eV according to UV–Vis analyses. The relationship between Urbach energy (E_U), skin depth (χ), steepness parameter (σ), refractive index (n), and other optoelectronic parameters with deposition pressure is thoroughly investigated. A correlation between the structural and optoelectronic properties of CdTe thin films and the deposition pressure in the Ar atmosphere of the as-deposited layers has been recognized through this study which is useful for designing and manufacturing CdTe solar cells and implies substantial commercial assurance.

Address correspondence to E-mail: bashar@agni.com

https://doi.org/10.1007/s10854-022-09603-w

1 Introduction

The development of high-performance and low-cost photovoltaic cells for nonconventional energy sources relying on the photovoltaic effect is currently a crucial scientific and technological issue [1]. Because of their potential applications in thin-film solar cells and other optoelectronic devices, binary II–VI compound semiconductors have piqued scientists' curiosity. Cadmium telluride (CdTe) is one of the most value-added materials in the II–VI group [2]. In a few micrometers of CdTe material, more than 90% of the incident light is absorbed. Due to the high absorption coefficient ($> 10^4$ cm^{-1}) and nearly ideal direct band gap (1.45 eV), light can be absorbed and converted to power in several-millimeter-thick CdTe layers, which may be produced on a variety of substrates, including glass, metallic foils, polymers, and ultra-thin glass, enabling conventional, lightweight, and adjustable design [3, 4]. Furthermore, theoretical evaluations of probable photovoltaic solar energy conversion into electricity for CdTe are around 29% [1]. Electrons often migrate between the conduction and valance bands of the same wave vector by collecting or releasing a photon without phonon interaction. As a result, high-quality CdTe thin films are widely employed in a variety of electrical and optoelectronic devices, covering solar cells, photodetectors, infrared windows, X-ray detectors, light-emitting diodes, lasers, and so on [5].

The quest for the CdS/CdTe heterojunction solar cell emerged early with a 6% power conversion efficiency [6]. Using the close-spaced sublimation (CSS) approach, Kodak laboratories reached 10% efficiency for CdTe thin-film solar cells in 1984 [3]. Another research group from South Florida University obtained 15.8% efficiency in 1993 when he utilized the CSS to deposit CdTe films on a borosilicate glass substrate at around 650 °C [7]. After a while, a team from the National Renewable Energy Laboratory (NREL) attained an efficiency of 16.5% [8]. CdTe thin-film solar cells have seen a considerable increase in efficiency from 16.5 to 22.1% between 2013 and 2016 [9]. According to First Solar Inc., current efficiency has approached 22.1% PCE [10]. The gap between the maximum theoretical efficiency (30%) and the highest measured laboratory efficiency (22.1%) of CdTe solar cells is being bridged by sustained research efforts.

Due to its low sublimation temperature, CdTe can be produced using a variety of processes, each of which has a substantial impact on the material's properties and device performance. Sputtering [4], CSS [5], vapor transport deposition (VTD) [10], thermal evaporation [11], co-sputtering [12] and electrodeposition [13] are some of the CdTe deposition processes and so on. CSS is one of the several strategies that have yielded positive results so far. High deposition rates and extensive raw material consumption are two advantages of the CSS process, resulting in reduced manufacturing expenses and competitive module costs. CSS is a low-cost method for depositing polycrystalline thin films because of its low working pressure (0.01–1 Torr) and uncomplicated configuration.

Deposition requirements such as evaporation rate, substrate temperature, source to substrate distance, and film thickness, as well as microfabrication technique, atmosphere, annealing, $CdCl_2$ treatment [14], and doping, all affect the structural, optical, electrical, and topographical attributes of CdTe thin films. Thin-film CdTe used in photovoltaic devices is polycrystalline in nature. Solar cells fabricated from a material with tailored crystallite size have photovoltaic efficiencies that rise with a grain size up to the point where the device's series resistance R_s is no longer influenced by the grain boundaries.

The boundaries between single-crystal grains are expected to have a substantial impact on the photovoltaic efficiency of CdTe/CdS solar cells. There is likely to be a large prevalence of defects (e.g., dangling bonds, dislocations) near grain boundaries, and impurities and stoichiometric excesses of Te may also migrate to the boundary [15]. In the CSS technique, a sensible, innovative approach to alter crystallite size might be the adjustment of sublimation chamber pressure by Ar gas which will control the rate of sublimation of source materials. In designing optimal CdTe thin-film solar cells, it is crucial to find the optimal deposition condition for the CdTe absorber layer, especially a perfect sublimation rate for the CSS method, to obtain desired stoichiometry of the film. To investigate the effect of deposition pressure on the characteristics of CdTe thin film, Amin et al. [16] observed CSS-deposited CdTe thin film grown in the range of 1 Torr to 200 Torr Ar pressure. Falcao et al. [17] demonstrated the limited adsorption rate at high pressure (0.1–20 Torr) using pure argon or a mixture of argon and oxygen. The major goal of this research is to use the CSS approach to build a thin (about 5–6 μm) pinhole-free CdTe film with comparatively

lower Ar deposition pressures from 250 to 1000 mTorr to discover a possible enhancement in the film's structural and optoelectrical attributes. According to the diffusion transport hypothesis, CSS-deposited CdTe is grown when Cd and Te atoms migrate to the substrate while diffusing and colliding with gas molecules. Later they are condensed on the substrate. According to this theory [18], the deposition rate is an inverse function of ambient gas pressure as high deposition pressure increases the likelihood of a collision by decreasing the mean free path (MFP). Therefore, X-ray diffraction, SEM, AFM, and UV–Vis spectrophotometer are used to investigate the physical features of as-deposited CdTe thin film with an emphasis on lower Ar pressure for solar cell application.

1.1 Experimentation

Initially, 2-mm-thin borosilicate glass (BSG) substrates were pre-cut with a dimension of 3 cm × 3 cm. The glass substrates were ultrasonically cleaned with a sequence of methanol–acetone–methanol–DI water for 10, 10, 10, and 20 min, respectively. After cleaning, samples were dried by a jet stream of industrial N_2 gas. Then all substrates were plasma cleaned inside a plasma chamber (CY-P5L-B). CdTe films were grown on the BSG by CSS method. The CSS system employed in this work consists of a quartz tube augmented by halogen lamps as a heat source, thermocouples, and PID controllers to monitor the source and substrate temperatures.

CSS is a technique of converting a solid into vapor at a high temperature in a vacuum chamber. Figure 1 shows a schematic of the CSS system that was developed for experimentation. If the source and substrate temperatures are the same, the deposition on the substrate will reach equilibrium, and the film will not be grown. In most cases, a shorter distance between the source and the substrate minimizes the risk of mass transfer loss during sublimation. The source and substrate temperatures were both scaled up at the same time until they finally diverged for a different amount of time, which is regarded as depositing time. The selection of deposition parameters is influenced by the specific deposition procedure [19]. The temperatures of the source and substrate [3], annealing [20, 21], the nature of the environment [22], the working pressure [5], and the chemistry of the source material are all critical performance parameters in the CSS method. Thus, the variables are intertwined. The deposition parameters in this study, such as source–substrate temperature, spacing, deposition duration, and pressure, were chosen based on optimization from previously reviewed literature, analytical approaches, empirical results, and in some cases, plausible assumptions. Figure 2a shows a source with CdTe powder, and Fig. 2b depicts the CdTe thin films.

The substrate and source are separated by 2 mm. The system is sustained at the set temperatures (source temperature: 625 °C, substrate temperature: 585 °C) by 2 kW halogen lamps. The thermocouples are engaged to monitor the temperatures of the substrate and source. The chamber is reserved at 250–1000mTorr (Ar) to generate the suitable deposition ambient. The argon gas is used to maintain an inert atmosphere inside the chamber.

The main goal of this research is to control film thickness around 5 µm toward stable pinhole-free CdTe thin films. By keeping other deposition parameters constant, deposition pressure is changed to achieve the desired film thickness.

Accordingly, the temperature was kept constant for both the source and the substrate throughout the film growth. The deposition time was 10 min for all pressure variations. Table 1 shows the deposition conditions of CdTe film grown via CSS.

1.2 Characterization

To investigate the microstructure, the fabricated CZTS films are subjected to the X-ray diffraction (XRD) technique. XRD configurations are verified with a GBC, EMMA diffractometer with Cu-Kα radiation beam at 1.5406 Å wavelength. The diffractometer is operated at 35 kV and 28mA. A UV–Vis spectrophotometer (Hitachi, UH4150) is employed to reveal the optical absorbance between 300 and 800 nm wavelengths. UH4150 is a spectrophotometer that inherits the optical system of the U-4100, renowned for its parallel beam and low polarization characteristics, which are ideal for assessing optical characteristics. Film thickness is calculated with a Surface Profilometer (Dektak, Bruker). DektakXT enables vital nanometer-level surface measurements for the microelectronics, semiconductor, solar, high-brightness LED, medical, and materials research industries. Film morphology is examined with an

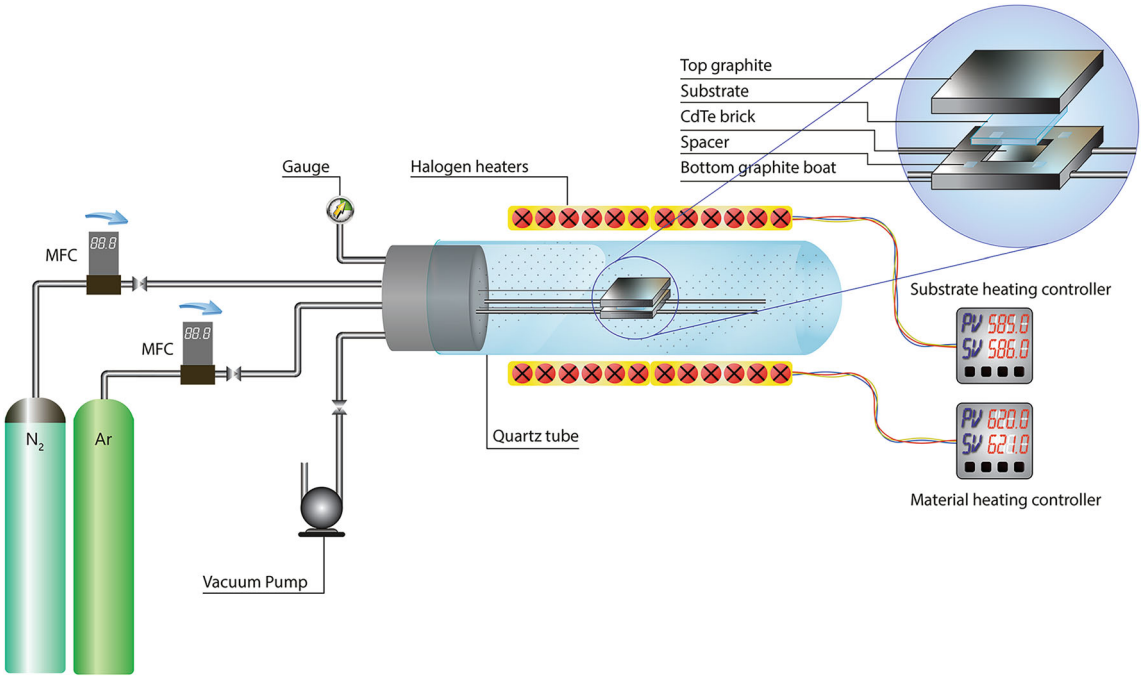

Fig. 1 Schematic diagram of a CSS system

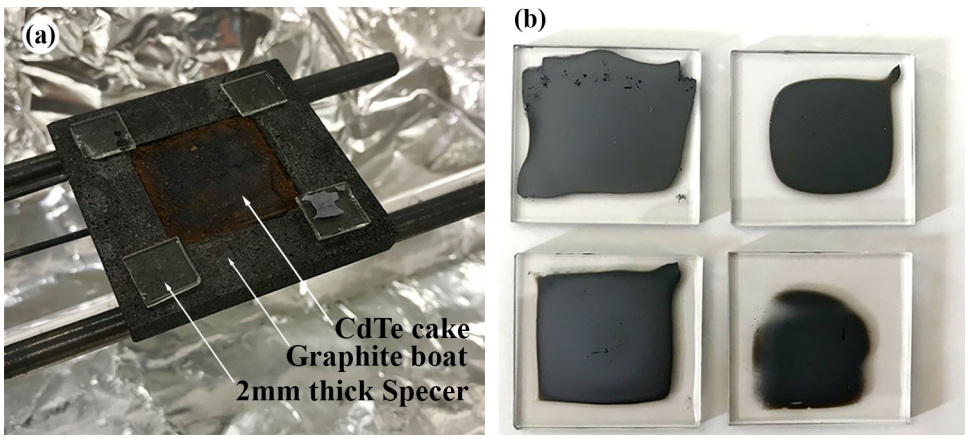

Fig. 2 **a** Source with CdTe powder and **b** CdTe-deposited substrate

Table 1 Different deposition conditions for CdTe thin-film growth and measured film thickness

Sample	Source temp	Substrate temp	Source–substrate spacing	Deposition time	Ar pressure (mTorr)	Film thickness, d (μm)
P250	625 °C	585 °C	2 mm	10 min	250	6.50
P500					500	5.20
P750					750	6.70
P1000					1000	6.00

atomic force microscope (Nanosurf, C3000) and scanning electron microscope (Zeiss, EVO18).

2 Results and discussion

2.1 Structural properties

The structural properties of as-grown CdTe thin film are studied by XRD. The XRD patterns of the aforementioned as-deposited films are shown in Fig. 3. It is observed from the XRD spectra that the CSS-deposited CdTe films show polycrystalline nature with the preferential orientation along with (1 1 1) plane and originated at $2\theta = 23.8°$ for all the deposition conditions approving a cubic construction. Additional two low-intensity peaks are noted at $2\theta = 39.30°$ and $2\theta = 46.51°$ corresponding to the (2 2 0) and (3 1 1) plane, respectively, which are well indexed with the JCPDS Card No. 03-065-1046 [23]. From the XRD peak, it is obvious that the pattern is dominated by the (1 1 1) peak as the intensity of the other two CdTe peaks (2 2 0) and (3 1 1) is very weak. All these films are polycrystalline with a cubic phase and are in settlement with the XRD consequences stated by previous studies [1, 19, 24].

The strongest preferred (1 1 1) orientation is seen in the sample deposited at 500 mTorr Ar pressure. After this deposition pressure, the peak intensity showed a diminishing trend, which may be attributed to the formation of successive thin layers of material and a decrease in surface mobility on the Borosilicate glass [2, 19]. To achieve similar intensity, the amount of deposited material has to be the same. If the thickness and deposition time is altered, the peak intensity may differ. Variations in XRD peak intensities are often linked to changes in the scattering intensity of crystal components or their lattice orientation and can be regarded as a result of crystallite size variations caused by a variety of events. It could also be caused by a discontinuity in the film texture, a high porosity in the samples, huge voids, or a rough substrate [25].

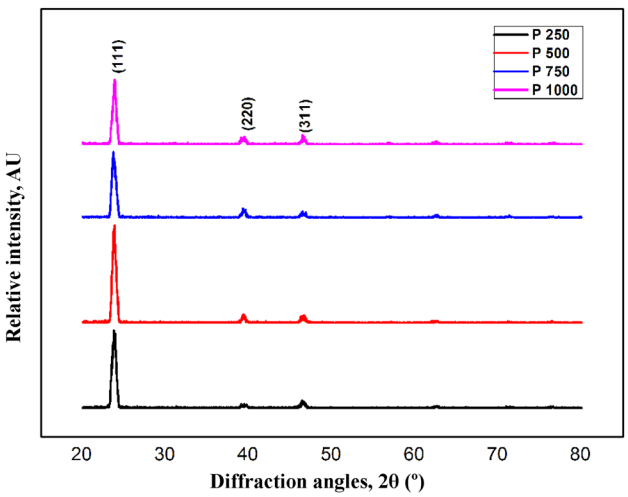

Fig. 3 XRD of as-deposited CdTe thin film

The regular crystallite size is assessed from the full width of half maximum (FWHM) of the utmost powerful peak (111) with the Scherrer formula

$$D = \frac{K\lambda}{\beta\cos\theta}, \quad (1)$$

where β is the full width of half maximum (FWHM) in radians, λ is the wavelength (1.54 Å), and $k = 0.89$ is the Scherrer constant. The estimated regular crystallite size, D, of the samples for the (111) plane is listed in Table 2. It is depicted here that the FWHM of the major diffraction peak decreases with increasing crystallite size, D. It is clear that the samples annealed at the lower pressure (P 250 and P 500) have comparatively lower FWHMs and larger crystallite sizes. For deposition, the source and substrate temperatures were maintained at 625 and 585 °C. Rising the temperature origins more mobility and diffusion of the surface, which permits the element to travel and unite together, resulting in superior regular crystallite size with a minor FWHM. However, Amin et al. [16] have reported a larger crystallite size (21–38 nm) for deposition pressure of 1–200 Torr where ultra-thin glass (UTG) is used as substrate. UTG is ideal as a substrate since it is very resistant to air and moisture, offers transparency and bendability, and possesses a thermal expansion coefficient (CTE) of $7.2 \times 10^{-6}\ K^{-1}$ near CdTe ($5.9 \times 10^{-6}\ K^{-1}$) [16]. However, we have used BSG as a substrate for this study and its CTE is $3.3 \times 10^{-6}\ K^{-1}$. The formation of any tensile or compressive stress during high temperature/pressure deposition, as well as cracks or shrinkage during the cooling period, is minimized with the aid of CTE equilibrium [26]. So, the use of UTG might have a great contribution to structural attributes along with lower Ar pressure.

The data of dislocation density, δ, shown in Table 2 are also lower for the samples with larger crystallite sizes indicating fewer lattice imperfections and decreased strain [27]. Still, the crystallite size does not seem to diverge considerably through rising Ar

Table 2 Structural parameters of CdTe thin films at various deposition pressures for (111) plane

Sample	Position, 2θ	d_{hkl} (Å)	FWHM (deg)	Crystallite size, D (nm)	Dislocation density, δ ($\times 10^{15}$) (lines/m^2)	Strain, ε ($\times 10^{-3}$)	Crystallite number, N m^{-2} ($\times 10^{14}$)
P 250	23.798	3.7358	0.527	16	3.87	2.92	8.98
P 500	23.748	3.7428	0.526	16	3.84	2.77	8.91
P 750	23.749	3.7429	0.544	16	4.11	2.86	9.87
P 1000	23.670	3.7554	0.549	15	4.20	2.67	10.22

pressure (250–1000 mTorr) as the crystallization temperature or annealing temperature shows a significant effect on the crystal morphology. Moreover, an additional tensile or compressive stress is present in the CdTe film due to the use of BSG as substrate [26] which has an impact on crystal structure and lattice strain.

The dislocation density δ [28] is defined as the number of dislocations per unit volume of a crystal. It can be estimated by

$$\delta = \frac{1}{D^2}. \tag{2}$$

Stress is one of the most vital factors influencing microstructural properties. The strains that arise in thin films deposited on substrates can jeopardize thin-film electronic device reliability. Understanding the origin of these stresses and the governing deformation processes in thin films is required in order to design these devices for greater mechanical reliability. In nanomaterials, crystal dislocation enhances strain. According to the Williamson–Hall isotropic strain model (W-HISM) [28, 29], the dimension of the crystallite and the strain in the lattice are unrelated. However, the Williamson–Hall anisotropic uniform deformation energy density model (W-HUDEDM) [30] states that when the crystallites are quite tiny, there are greater volume defects at grain borders. A stress field is created by the internal pressure exerted by surface tension due to volume defects. The strain in the lattice is caused by the extra stress at grain boundaries. Generally, the strain ε of the thin film is dignified as [31]

$$\varepsilon = \frac{\beta \cot\theta}{4}. \tag{3}$$

In addition, the crystallite number N can be calculated [32] by utilizing values of film thickness (d) and crystallite size, D *as*

$$N = \frac{d}{D^3}. \tag{4}$$

The value of microstructural parameters of position (2θ), d_{hkl}, FWHM, dislocation density, δ, strain, ε, and crystallite number, N is listed in Table 2.

2.2 Surface morphology

Scanning electron microscopy (SEM) is helpful in ensuring that huge areas of material are covered uniformly. This approach can be used to determine the existence of various surface defects and Te precipitation in CdTe. Figure 4 illustrates the SEM micrograph of a CSS-deposited CdTe layer with different Ar deposition pressures at a magnification of 25k to show consistent coverage. The premise, outcomes, and order of magnitudes of several approaches, for grain size calculation such as the Scherer formula and the Williamson–Hall plot, make it tough to compare them directly. However, all available techniques are capable of estimating accurate grain size to some extent [3, 19]. The size of crystalline domains is computed using XRD, whereas actual grains are visible using SEM.

As may be seen in SEM pictures, films have a homogeneous, smooth, and uniform surface with no pits or cracks (Fig. 4). For deposition pressures of 250 and 500 mTorr, some large grains can be seen alongside small grains in Fig. 4a and b. In Fig. 4c and d, the grains are nearly identical and densely packed, with smaller grains appearing at higher pressures of 750 and 1000 mTorr. Smaller grains are more reactive and have a higher solubility in melted flux, resulting in more efficient mass movement during annealing or post-heat treatment. For all CdTe films, there are no voids or inclusions, and the surface appears to be well ordered. And eventually, the XRD outcomes are supported by these SEM pictures.

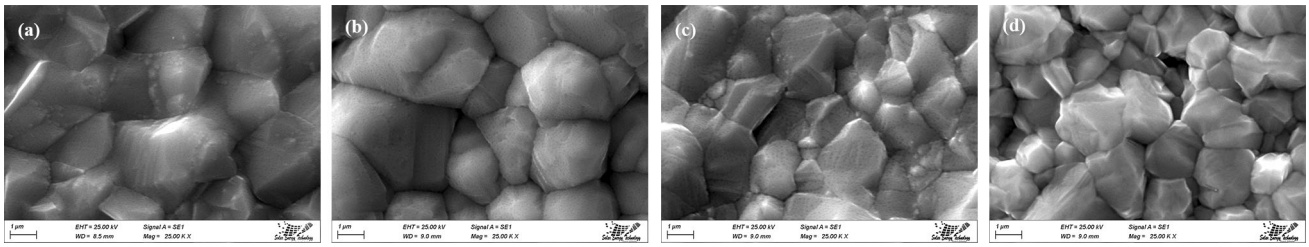

Fig. 4 SEM images of CdTe thin-film samples: **a** P 250, **b** P 500, **c** P 750, **d** P 1000

2.3 Surface topography

The surface topology of a thin film may be detected and visualized by AFM [14]. CSS-grown CdTe film is generally rough and has poor coverage. Therefore, AFM analysis is used to investigate the relationship between the roughness of CdTe thin films and their deposition pressure. Consequently, surface topography, average roughness (Ra), and RMS (Rq) roughness are all measured for this study using AFM. Figure 5 depicts the AFM surface topography of CdTe thin-film samples. In addition, Fig. 6 illustrates the topography (from a 3D image) of CdTe film in a scanning area of 20 μm × 20 μm for deposition pressure of 250, 500, 750, and 1000 mTorr, respectively.

Table 3 shows the variation of grain size, RMS roughness (Rq), and average roughness (Ra) achieved from the AFM study with the change in deposition pressure of CSS-deposited CdTe thin film. Crystallite size, according to the literature, is a measurement of the size of coherently diffracting regions of material. The Scherrer equation is widely used to calculate the crystallite size from an XRD pattern. Grains, on the other hand, refer to the average diameter of the individual crystal orientations. Grain is a single-crystalline or polycrystalline material that can be found in bulk or as thin films. Due to kinetics, smaller crystallites move closer during processing and become larger. As a result, the grain is more than likely larger than a crystallite. If the grain is exactly single crystallite, crystallite size equals grain size [19]. Table 3 shows that grain size changes with deposition pressure. For the lowest deposition pressure at 250mTorr, the grain size was the largest (2.21 μ*m*). And it decreases with increasing deposition pressure of Ar. Nevertheless, Major et al. [5] demonstrate another study of grain size controlling of CdTe thin film where N_2 pressure was varied (2–200 Torr) and the range of grain sizes increased with N_2 pressure. However, The AFM data support the hypothesis of improved grain size for lower deposition pressure by XRD and SEM for this study.

The roughness of the surface indicates its level of homogeneity. Both average roughness, Ra, and RMS roughness, Rq, calculate the roughness of thin films, but their mechanisms for that are distinct. Increased roughness causes greater light scattering, which can result in higher reflectance or even attenuation. To create a longer optical length, more roughness is recommended. The changes in surface roughness could be attributed to surface flaws, changes in the degree of disorder, and the porosity of the films [33]. In addition, for this study, the mean roughness (Ra) values are in the range of 199–293 nm which is in accordance with the study accomplished by Seth et al. [19, 34].

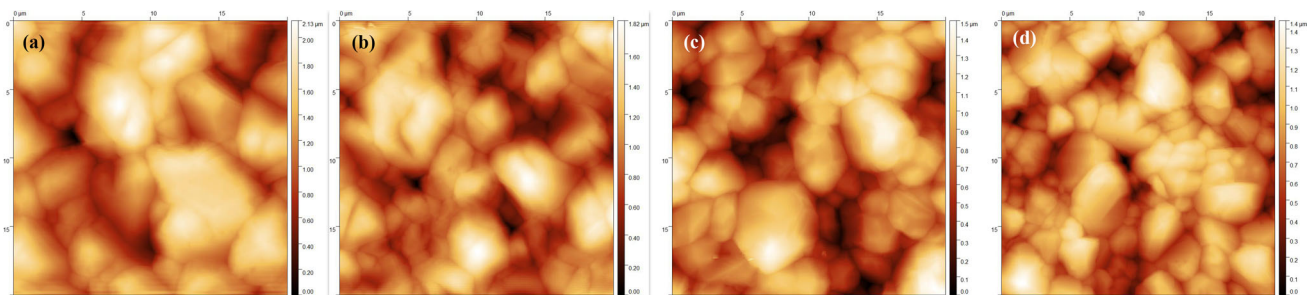

Fig. 5 Surface morphology of CdTe thin film by using AFM: **a** P 250, **b** P 500, **c** P 750, **d** P 1000

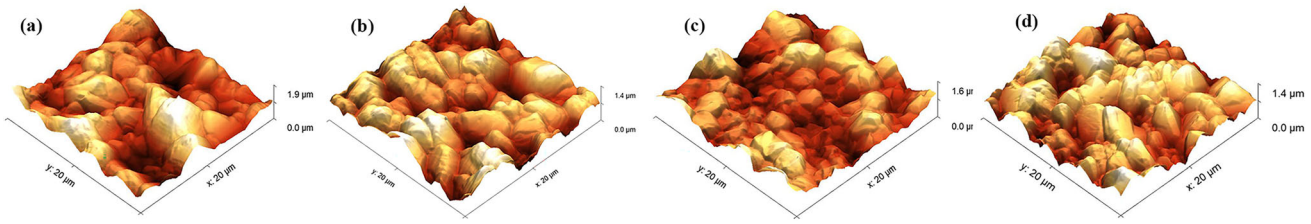

Fig. 6 3D images of CdTe thin film by using AFM: **a** P 250, **b** P 500, **c** P 750, **d** P 1000

Table 3 RMS roughness (Rq) and mean roughness (Ra) of CdTe thin film from AFM analysis

Sample	Grain size μm	RMS roughness (Rq) nm	Mean roughness (Ra) nm
P 250	2.21	356.99	293.52
P 500	1.76	312.37	251.54
P 750	1.63	262.10	213.82
P 1000	1.48	245.47	199.86

2.4 Optical properties

2.4.1 *Transmittance (%T), and absorption coefficient (α)*

The absorbance of deposited CdTe thin films is assessed by measuring optical properties. To normalize the impact of the underlying substrate, the reference glass' absorbance is deducted. Figure 7 illustrates the transmittance (%T) spectra of CdTe thin films. The UV–Vis spectra of the CZTS samples portrayed in Fig. 8 show that the CdTe thin films possess high optical absorbance with a large absorption coefficient, α, where the transmission and reflection losses have been discounted. The measured absorption coefficient values for all the samples are $> 10^4\ \mathrm{cm}^{-1}$ in the visible region which confirms the absorbance of more than 90% as desired for an effective absorber layer [28, 31] for the absorption coefficient:

$$\alpha = \frac{A(h\nu - E_g)^n}{h\nu}. \tag{5}$$

Here, n is the constant number having values 1/2, 2, 3/2, or 3 corresponding to allowed direct, allowed indirect, forbidden direct, or forbidden indirect transitions, respectively, and the remaining have their usual meanings. The absorption coefficient α [27, 28] is estimated by means of the following relation from the absorbance A as

$I = I_o e^{-\alpha d}$, or

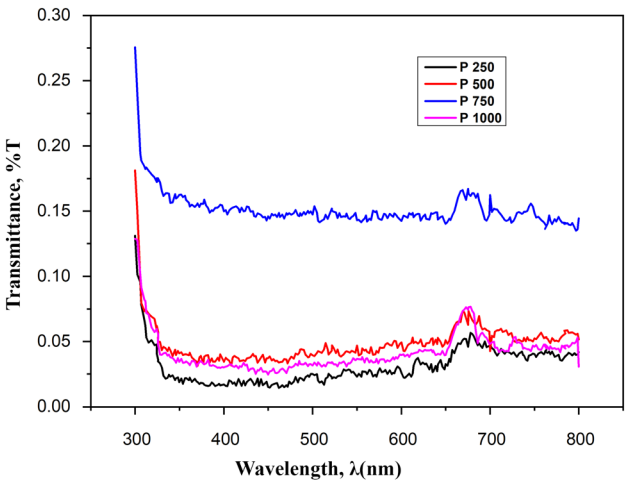

Fig. 7 Transmittance spectra (%T) of CdTe thin-film samples: (a) P 250, (b) P 500, (c) P 750, (d) P 1000

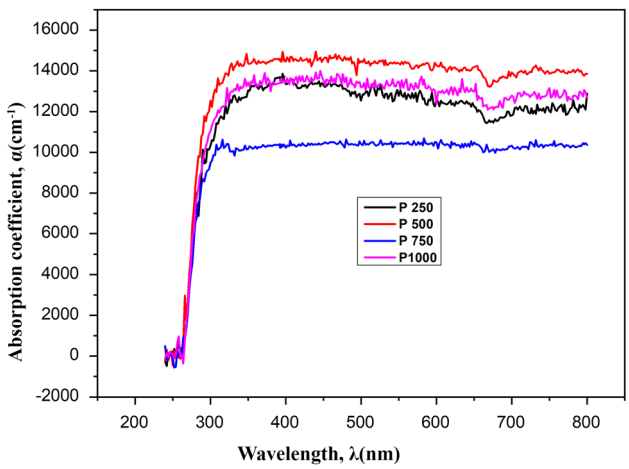

Fig. 8 Absorption coefficient α of CdTe thin-film samples: (a) P 250, (b) P 500, (c) P 750, (d) P 1000

$$\alpha = 2.303\left(\frac{A}{d}\right), \tag{6}$$

where I expresses the transmitted intensity, I_o expresses the incident intensity, A is the absorbance, and d is the width of the fabricated film.

2.4.2 Band gap energy (E_g)

The graphs of $(\alpha h\nu)^2$ vs. hν are plotted in Fig. 9 to define the energy band gaps of the films. The optical absorbance and band gap allocation of films are greatly affected by the grain homogeneity of the substrate surface. The Tauc plot's appearance verifies CdTe's status as a direct band gap semiconductor. The energy band gap is measured in the region of 1.45–1.55 eV and changes in the band gap are linked to changes in Cd stoichiometry and crystallinity [35, 36]. The Burstein–Moss effect clarifies that changes in the absorption shift and carrier concentration may result in changes in the band gap too [37]. Strong interaction between the substrate and vapor atoms on samples is the other factor of band gap reduction in the case of treated CdTe. The adjustment in the optical band gap could be due to a change in base pressure initiated by a change in film stoichiometry, which reasons changes in electrical characteristics like carrier density and mobility. Dislocation density (δ), disorder at grain boundaries, stoichiometric deviations, quantum size impact, and change in preferred orientation can all affect the band gap of a semiconductor material [19]. However, our experimental data are in good agreement with the study [38] which reported that the direct optical band gap of CdTe thin film was approximately 1.65 eV before treatment and 1.5 eV after treatment.

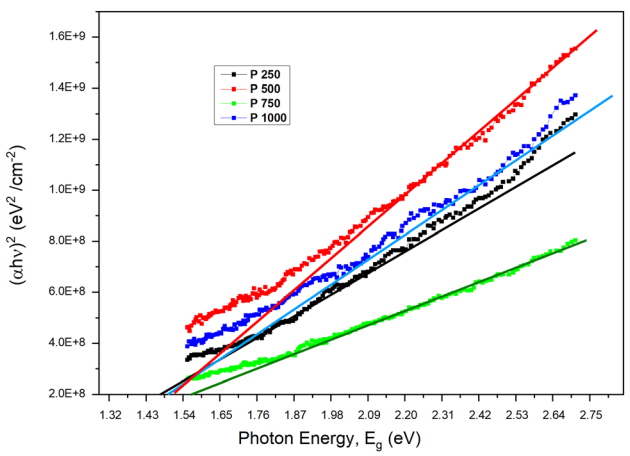

Fig. 9 Plot of $(\alpha h\nu)^2$ versus photon energy ($h\nu$) for the band gap calculation of CdTe thin films

2.4.3 Urbach energy (E_U), steepness parameter (σ), extinction coefficient (K), and skin depth (χ)

The ultimate absorption edge beneath the energy band gap (E_g) rises exponentially in semiconductors and insulators, and this absorption edge is denoted as the Urbach tail [39]. Over the years, researchers have looked at the actual cause of Urbach tails in semiconductor materials.

The width of the defect bands created as an intermediate state in the band gap of CdTe can be determined. These defect band states produce a band tail that extends from the lower conduction band to the higher valence band. As a result, an energy tail forms on both sides of the valence band maximum and conduction band minimum [40, 41]. In amorphous, disordered, and crystalline materials, the tail emerges toward the optical band edge. According to research, such tails are caused by strains high enough to drive local states past the band edges and decay exponentially into the band gap [42]. According to the study, phonons, excitons, impurities in crystal, and structural irregularities in the lattice have been linked with the detected tails, which are mathematically exponent.

The spectrum dependence of absorption coefficient (α) with photon energies ($h\nu$) less than the energy band gap of a CdTe thin film is determined by

$$\alpha = \alpha_0 e^{\frac{E}{E_0}}, \tag{7}$$

where α_0 is a constant and E_U is the Urbach energy. In the energy spectrum of the absorption coefficient, the Urbach tail is an exponential portion. The degree of structural disorder in thin films is measured by Urbach energy (E_U). The local defect or localized states at the optical energy gap are represented by this quantity. Electronic transitions between localized states may cause the optical absorption coefficient (α) of thin films to be dependent on photon energy [4]. In Fig. 10, we show the logarithmic absorption coefficient (α) of the CdTe film as a function of wavelength (λ). The reciprocal of the slopes of the linear portion, below the optical band gap, gives the value of E_U. The values of the E_U are listed in Table 4. The experimental value of the E_U is much higher than the reported data [16]. Crystal defects may be the cause

of a spike in Urbach energy, which causes the localized state to reorganize in thinner samples.

The number of thermally produced phonons is very low at low temperatures; hence, E_U's weak temperature dependency is primarily due to structural abnormalities. Due to the presence of a considerable quantity of unanticipated impurities and vacancies, the thin film is acknowledged to have a major number of structural abnormalities. Based on the influence of structural disorder and thermal effect on the electronic attributes of silicon, Cody et al. [43] developed a model for the Urbach energy (E_U). In this study, all the CdTe samples are fabricated at the same temperature. So the value of Urbach energy has not been seen to vary drastically.

Meanwhile, in Wasim's model [44], the Urbach energy of Cu ternaries fluctuates from Cody's by one extra variable that accounts for phonon(s)–exciton(s) interaction. The intensified interaction between electron and phonon occurs as the number of phonons grows with rising temperature causing a larger temperature dependency of E_U in the high-temperature zone. At high temperatures, the electron–phonon interaction governs the temperature reliance of Urbach energy, E_U. Furthermore, these two effects are additive and have a significant impact on absorption tails [39].

The *steepness parameter* [39, 45] $\boldsymbol{\sigma}$ characterizing the broadening of the optical absorption edge due to electron–phonon interactions can be determined by

Equation	y = a + b*x			
Plot	P 250	P 500	P 750	P1000
Intercept	7.63665 ± 0.56482	9.38301 ± 0.53116	9.7036 ± 0.53336	9.18988 ± 0.45078
Slope	4.22075 ± 0.3808	3.14282 ± 0.35811	2.74978 ± 0.35959	3.18137 ± 0.30392

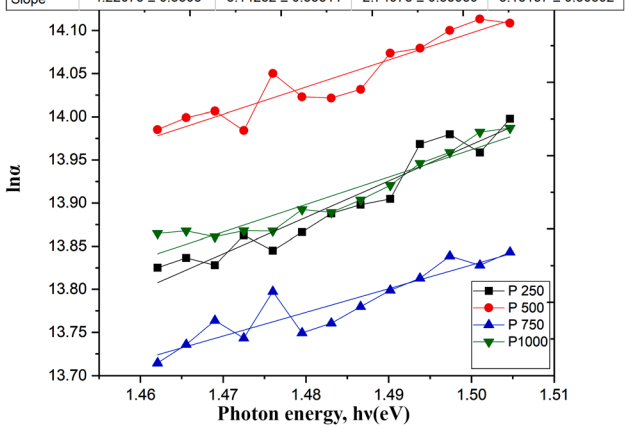

Fig. 10 Plot of Ln α as a function of the incident photon energy of CdTe thin film deposited at different pressures

$$\sigma = \frac{kT}{E_U}, \tag{8}$$

where k denotes the Boltzmann constant and T denotes the absolute temperature. The impact of impurities and disorders on the Urbach tail is not incorporated here. The calculated values of σ of CdTe films are listed in Table 4.

Extinction coefficient (K) is a study of light lost due to scattering and absorption per unit volume of the medium through which it passes [46]. The mass density or molar concentration of a specific material determines the absorbance of light at a given wavelength. So, the extinction coefficient (K) depends on the material and also on the photon energy [47]. The depth of material necessary to absorb half of the incident energy is 0.693/K. The extinction coefficient (K) can be expressed by

$$\alpha = \frac{4\pi K}{\lambda}. \tag{9}$$

Figure 11 shows the dependence of the extinction coefficient K of CdTe thin film deposited at different pressures. The value of the extinction coefficient K was less in the ultraviolet region, but it increases linearly with the increment of wavelength (λ) in the visible region. In addition, it shows a higher value of extinction coefficient K for the sample deposited at a pressure of 500 mTorr and lowest for the sample deposited at 750 mTorr. As it is directly proportional to absorbance coefficient (α) and material thickness (d), this behavior is potentially in agreement with the same rationale mentioned in Table 1; Fig. 8. Lower extinction coefficient values represent the comparatively smoother surface of thin film and lower loss of light energy by scattering and absorption.

Another crucial metric linked to light absorption within the thin film is *skin depth*, $\boldsymbol{\chi}$ (also known as penetration depth). It is the thickness at which the photon density equals 1/e of the surface value. It is determined by the conductivity of the thin films under study and the wavelength of the incident light. The optical characteristics of semiconducting materials can be related to skin depth [48, 49]. Due to the substantial dependence of conductivity in semiconducting materials on the optical band gap, the skin depth may be calculated as [48, 50].

Table 4 Optical parameters of CdTe thin films

Sample	Band gap, E_g (eV)	Urbach energy, E_U (eV)	Steepness parameter, σ x (10^{-2})	Refractive index, n	High-frequency dielectric constant, ε_∞	Dielectric constant, ε_o
P 250	1.45 ± 0.01	0.24	10.90	2.938 ± 0.004	8.630	14.054 ± 0.025
P 500	1.52 ± 0.02	0.32	8.12	2.903 ± 0.006	8.429	13.838 ± 0.038
P 750	1.55 ± 0.01	0.36	7.11	2.889 ± 0.004	8.347	13.746 ± 0.025
P 1000	1.48 ± 0.02	0.31	8.22	2.923 ± 0.008	8.542	13.962 ± 0.052

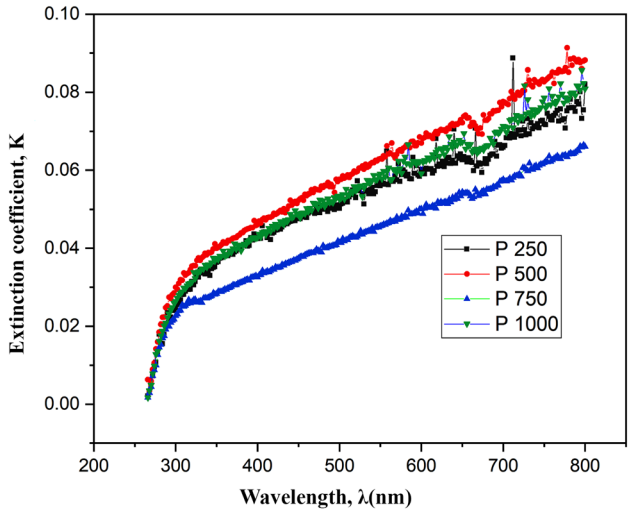

Fig. 11 Dependence of the extinction coefficient (K) of CdTe thin films on the wavelength (λ) of incident light

$$\chi = \frac{1}{\alpha}. \tag{10}$$

Here, χ is the skin depth, and α is the thin film's absorption coefficient. Skin depth is related to the square root of the resistivity in a good conductor. As a result, better conductors have a shallower skin depth. Figure 12 depicts the skin depth dependence on incident light wavelength for close-spaced sublimated CdTe thin films. The value of skin depth χ was high in the ultraviolet region and it decreases drastically and becomes stable with the increment of wavelength (λ) in the visible region. Moreover, the plot illustrates that skin depth χ is lower for films with higher absorbance. And that is obvious because high absorption causes the film's transmittance to decrease, allowing the light wave to travel less through the film.

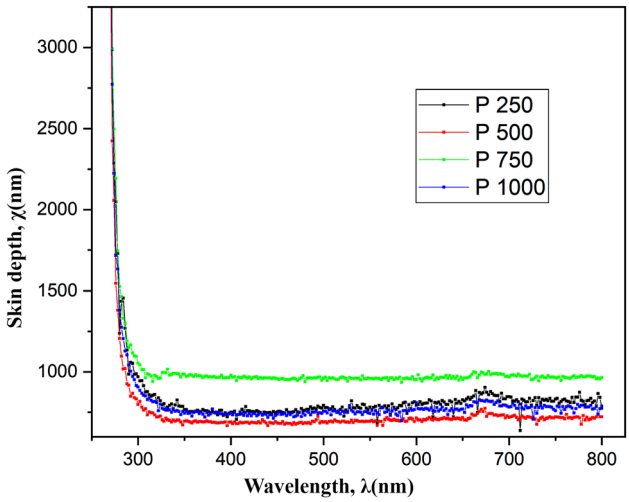

Fig. 12 Dependence of Skin depth (χ) of CdTe thin films on the wavelength (λ) of incident light

2.4.4 *Refractive index (n), high-frequency dielectric constant (ε_∞), and static dielectric constant (ε_o)*

Due to the difficulties of employing experimental equipment to assess the electric characteristics at higher temperatures, the dielectric properties of II–VI semiconductors are measured primarily based on low temperatures [51]. In order to enhance their application for thermoelectric devices, this theoretical study is a complement to semiconductor material research. The refractive index (n) of the thin film is one of the foremost factors in the prospect of total internal reflection inside a photovoltaic cell [52]. The refractive index, which is defined as a measure of density, also provides information regarding voids in the deposited layer [10]. The refractive index usually increases as the optical energy band gap reduces, and the two factors can be connected using the Harve–Vandamme model [11]. However, for simplicity, the refractive index n of CdTe thin films fabricated for

the communication is considered from the Moss relation [28]

$$E_g n^4 = k, \tag{11}$$

where k denotes a constant with a worth of 108 eV. The E_g varies from 1.45 to 1.55 eV for this experiment, whereas it varies from 1.66 to 1.69 eV reported by Amin et al. [16]. Repelling electrons and/or passivation defects that act as recombination sites at the interface are minimized by a narrower band gap range. The relation between band gap energy (E_g), refractive index (n), and dielectric constant (ε) of CdTe thin film is depicted in Fig. 13.

The dielectric belongings of material are related to its capacity to obstruct an electron's mobility when it is polarized under the inspiration of an exterior electric field. The dielectric constant is modified by electromagnetic radiations moving through the material and is influenced by the sensitivity of the electronic structure of the semiconductor. Materials with appropriate dielectric constants are beneficial to develop efficient solar cells [10].

The high-frequency dielectric constant ε_∞ of CdTe film is estimated by the following equation [27]

$$\epsilon_\infty = n^2. \tag{12}$$

The static dielectric constant, ε_o of each thin film [31] is calculated using the relation

$$\varepsilon_o = 18.52 - 3.08E_g. \tag{13}$$

The value band gap, refractive index, and dielectric constant of the CdTe thin films deposited in different Ar pressures are revealed in Table 4. All the values are in decent settlement with former reports [19, 20].

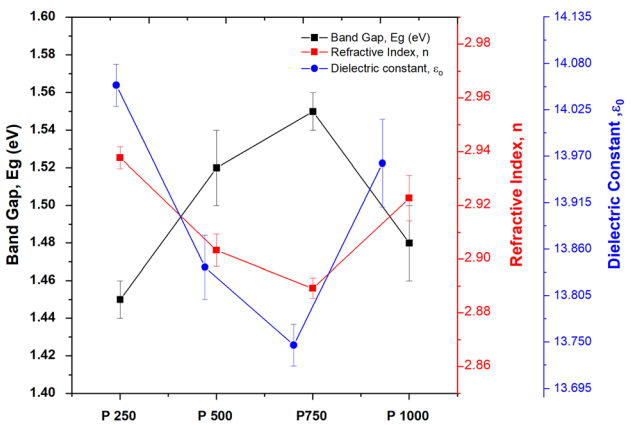

Fig. 13 Band gap energy (E_g), refractive Index (n) and dielectric constant (ε) of CdTe thin film fabricated at diverse pressure

3 Conclusion

In this study, CdTe thin films were grown on borosilicate glass substrates via a high-temperature deposition process called CSS. The deposition pressure (Ar) varied from 250 to 1000 mTorr. The impact of deposition pressure (Ar) on the physical properties of CdTe thin films has been inspected comprehensively. The polycrystalline CdTe structure is acquired with a sharp peak at (111), (220), and (311) planes. The crystalline nature difference was discovered at various deposition pressure. The variation of crystallite size (D), dislocation density (δ), strain (ε), and crystalline number (N) has been listed to observe the significance of deposition pressure on the CdTe thin film. The findings reveal that altering the pressure of inert gas (Ar) present during the formation of CSS-deposited CdTe films can result in a considerable microstructural change. Comparatively larger crystallite size is obtained for lower deposition pressure which is revealed by XRD analysis and it is in agreement with SEM and AFM analysis. The contribution to series resistance R_s from grain borders may be predicted to diminish as grain size increases. As a result, the performance of solar cells may steadily improve. The grain size management method used in this study can be used to do a schematic evaluation of solar cell performance using grain size as the only parameter. Surface roughness is distorted by the deposition pressure and depicts a relatively less roughness value for higher deposition pressure (750 and 1000 mTorr). Band gap energy (E_g) of CdTe thin film varies from 1.45 to 1.55 eV which is ideal for the absorber layer of the solar cell. The refractive index (n) was found in the range of 2.88–2.93. A fixed temperature is maintained for all CdTe sample fabrication, so there is no orientation in the calculated Urbach energy (E_U) or steepness parameter (σ). Hereafter the weak temperature reliance of Urbach energy E_U is predominantly accompanied by impurities and thermal and structural disarrays. However, the inquiry of the Urbach effect in the optical absorption spectra of the CdTe thin films deposited by CSS is reported here for understanding. This will be fascinating to examine how Cu-doped CdTe thin films compete with as-deposited films in terms of

absorption edges; as such, results will help explain the exact function of impurities and disorders in the optical attributes of CdTe thin films. As a result, it is concluded that deposition pressure has a significant impact on CdTe thin-film attributes. Furthermore, all of the examined features of CdTe thin films are well matched within the range of typical reported values, indicating that they have the aptitude to be used as absorber layers in solar applications. The selection of the ideal substrate for CdTe thin-film solar cells can be further improved by micromechanical analyses of the interface and coating strength incorporating selective chlorine treatment.

Author contributions

MSB was involved in conceptualization, visualization, and supervision; AS and MS carried out formal analysis; AS undertook the investigation and wrote and prepared the original draft; SSM curated the data; and MAAS and SA were responsible for project administration. All authors have read and agreed to the published version of the manuscript.

Funding

This work was supported by the Bangladesh Council of Scientific and Industrial Research, Ministry of Science and Technology, Bangladesh, through the research and development project grant scheme (ref: 39.02.0000.011.14.134.2021.388; dt: 21-09-2021) titled 'Increasing the photo-conversion efficiency of CdTe-based solar cell by selective Cl-treatment.'

Data availability

The datasets generated during and/or analyzed during the current study are available from the corresponding author on reasonable request.

Declarations

Conflict of interest The authors declare no conflict of interest.

References

1. N. Spalatu, J. Hiie, V. Valdna, M. Caraman, N. Maticiuc, Energy Procedia **44**, 85 (2020)
2. S. Chander, M.S. Dhaka, Results Phys. **8**, 1131 (2018)
3. C. Doroody, K.S. Rahman, S.F. Abdullah, M.N. Harif, H.N. Rosly, S.K. Tiong, N. Amin, Results Phys. **18**, 103213 (2020)
4. M.A. Islam, K.S. Rahman, K. Sobayel, T. Enam, A.M. Ali, M. Zaman, M. Akhtaruzzaman, N. Amin, Sol. Energy Mater. Sol. Cells **172**, 384 (2017)
5. J.D. Major, Y.Y. Proskuryakov, K. Durose, G. Zoppi, I. Forbes, Sol. Energy Mater. Sol. Cells **94**, 1107 (2010)
6. S.L. Patel, S. Himanshu, M.D. Chander, Kannan, M.S. Dhaka, Phys. Lett. Sect. A Gen. At. Solid State Phys. **383**, 1778 (2019)
7. A. You, M.A.Y. Be, I. In, 2851 (2018)
8. J.C.K.X. Wu, R.G. Dhere, C. DeHart, D.S. Albin, A. Duda, T.A. Gessert, S. Ashar, D.H. Levi, P. Sheldon, in Proceedings of the 17th European PVSEC 995 (2001)
9. I.M. Dharmadasa, A.A. Ojo, J. Mater. Sci. Mater. Electron. **28**, 16598 (2017)
10. S. Chander, A. Purohit, C. Lal, M.S. Dhaka, Mater. Chem. Phys. **185**, 202 (2017)
11. S. Chander, M.S. Dhaka, J. Mater. Sci. Mater. Electron. **27**, 11961 (2016)
12. M.A. Islam, K.S. Rahman, F.M.T. Enam, K. Sobayel, I. Kamaruzzaman, M. Akhtaruzzaman, N. Amin, Chalcogenide Lett **15**, 293 (2017)
13. A.A. Ojo, I.M. Dharmadasa, J. Mater. Sci. Mater. Electron. **28**, 14110 (2017)
14. S.L. Patel, S. Chander, A. Purohit, M.D. Kannan, M.S. Dhaka, J. Phys. Chem. Solids **123**, 216 (2018)
15. A. Morales-Acevedo, Sol. Energy **80**, 675 (2006)
16. N. Amin, M.R. Karim, Z.A. Alothman, Coatings **12**, 589 (2022)
17. V.D. Falcão, W.A. Pinheiro, C.L. Ferreira, L.R. de Oliveira Cruz, Mater Res **9**, 29 (2006)
18. Q.G. Zhang, X. Zhang, B.Y. Cao, M. Fujii, K. Takahashi, T. Ikuta, Appl. Phys. Lett. **89**, 114102 (2006)
19. K.S. Rahman, M.N. Harif, H.N. Rosly, M.I. Bin Kamaruzzaman, M. Akhtaruzzaman, M. Alghoul, H. Misran, N. Amin, Results Phys. **14**, 102371 (2019)
20. H.N. Rosly, K.S. Rahman, M.N. Harif, C. Doroody, M. Isah, H. Misran, N. Amin, Superlattices Microstruct. **148**, 106716 (2020)
21. E.M.K. Ikball Ahamed, A.K. Sen Gupta, M.N.I. Khan, M.A. Matin, N. Amin, in 2020 IEEE Region 10 Symposium TENSYMP 2020, p. 1168 (2020)

22. M. Green, K. Emery, Y. Hishikawa, W. Warta, E. Dunlop, D. Barkhouse, O. Gunawan, T. Gokmen, D. Mitzi, IEEE Trans. Fuzzy Syst. **20**, 1114 (2012)
23. S. Najafi, M. Safari, S. Amani, K. Mansouri, M. Shahlaei, J. Mater. Sci. Mater. Electron. **30**, 14233 (2019)
24. I.M. Dharmadasa, P.A. Bingham, O.K. Echendu, H.I. Salim, T. Druffel, R. Dharmadasa, G.U. Sumanasekera, R.R. Dharmasena, M.B. Dergacheva, K.A. Mit, K.A. Urazov, L. Bowen, M. Walls, A. Abbas, Coationgs **4**, 380 (2014)
25. M. Inoue, I. Hirasawa, J. Cryst. Growth **380**, 169 (2013)
26. G. Abadias, E. Chason, J. Keckes, M. Sebastiani, G.B. Thompson, E. Barthel, G.L. Doll, C.E. Murray, C.H. Stoessel, L. Martinu, J. Vac. Sci. Technol. A Vac. Surf. Film **36**, 020801 (2018)
27. A. Sharmin, M.S. Bashar, S. Tabassum, Z.H. Mahmood, Int. J. Thin Film Sci. Technol. **8**, 67 (2019)
28. A. Sharmin, M.S. Bashar, M. Sultana, S.M.M. Al Mamun, AIP Adv. **10**, 015230 (2020)
29. P. Muhammed Shafi, A. Chandra Bose, AIP Adv. **5**, 057137 (2015)
30. R. Yogamalar, R. Srinivasan, A. Vinu, K. Ariga, A.C. Bose, Solid State Commun. **149**, 1919 (2009)
31. A. Sharmin, S. Tabassum, M.S. Bashar, Z.H. Mahmood, J. Theor. Appl. Phys. **13**, 123 (2019)
32. T. Shrividhya, G. Ravi, Y. Hayakawa, T. Mahalingam, J. Mater. Sci. Mater. Electron. **25**, 3885 (2014)
33. S. Chandramohan, R. Sathyamoorthy, P. Sudhagar, D. Kanjilal, D. Kabiraj, K. Asokan, V. Ganesan, J. Mater. Sci. Mater. Electron. **18**, 1093 (2007)
34. A. Seth, G.B. Lush, J.C. McClure, V.P. Singh, D. Flood, Sol. Energy Mater. Sol. Cells **59**, 35 (1999)
35. C. Kim, M. Daraselia, J. Garland, S. Sivananthan, Phys. Rev. B **56**, 4786 (1997)
36. G. Kartopu, O. Oklobia, D. Turkay, D.R. Diercks, B.P. Gorman, V. Barrioz, S. Campbell, J.D. Major, M.K. Al Turkestani, S. Yerci, T.M. Barnes, N.S. Beattie, G. Zoppi, S. Jones, S.J.C. Irvine, Sol. Energy Mater. Sol. Cells **194**, 259 (2019)
37. Z.M. Gibbs, A. Lalonde, G.J. Snyder, New J. Phys. **15**, 075020 (2013)
38. A.V. Kokate, M.R. Asabe, P.P. Hankare, B.K. Chougule, J. Phys. Chem. Solids **68**, 53 (2007)
39. R.C. Rai, J. Appl. Phys. **113**, 153508 (2013)
40. B. Choudhury, M. Dey, A. Choudhury, Int. Nano Lett. **3**, 2 (2013)
41. M.S. Bashar, R. Matin, M. Sultana, A. Siddika, M. Rahaman, M.A. Gafur, F. Ahmed, J. Theor. Appl. Phys. **14**, 53 (2020)
42. F. Urbach, Phys. Rev. **92**, 1324 (1953)
43. G.D. Cody, T. Tiedje, B. Abeles, B. Brooks, Y. Goldstein, Phys. Rev. Lett. **47**, 1480 (1981)
44. A. You, M.A.Y. Be, I. In, **5823**, 4 (2013)
45. H. Mahr, Phys. Rev. **125**, 1510 (1962)
46. A.S. Hassanien, J. Alloys Compd. **671**, 566 (2016)
47. Z. Berk, *Food Process Engineering and Technology* (Academic Press, Cambridge, 2013), p.607
48. C.M. Chen, Z.K. Lin, W.J. Huang, S.H. Yang, Nanoscale Res. Lett. **11**, 1–11 (2016)
49. V.K. Tomer, S. Duhan, Appl. Phys. Lett. **106**, 063105 (2015)
50. M.S. Bashar, R. Matin, M. Sultana, A. Siddika, M.A. Gafur, A. Farid, J. Nano Res. **70**, 27 (2021)
51. J.-C. Li, L.-S. Li, W. Sun, Procedia Comput. Sci. **174**, 673 (2020)
52. R.S. Dubey, S. Saravanan, S. Kalainathan, AIP Adv. **4**, 127121 (2014)

Terms and Conditions

Springer Nature journal content, brought to you courtesy of Springer Nature Customer Service Center GmbH (“Springer Nature”).
Springer Nature supports a reasonable amount of sharing of research papers by authors, subscribers and authorised users (“Users”), for small-scale personal, non-commercial use provided that all copyright, trade and service marks and other proprietary notices are maintained. By accessing, sharing, receiving or otherwise using the Springer Nature journal content you agree to these terms of use (“Terms”). For these purposes, Springer Nature considers academic use (by researchers and students) to be non-commercial.
These Terms are supplementary and will apply in addition to any applicable website terms and conditions, a relevant site licence or a personal subscription. These Terms will prevail over any conflict or ambiguity with regards to the relevant terms, a site licence or a personal subscription (to the extent of the conflict or ambiguity only). For Creative Commons-licensed articles, the terms of the Creative Commons license used will apply.
We collect and use personal data to provide access to the Springer Nature journal content. We may also use these personal data internally within ResearchGate and Springer Nature and as agreed share it, in an anonymised way, for purposes of tracking, analysis and reporting. We will not otherwise disclose your personal data outside the ResearchGate or the Springer Nature group of companies unless we have your permission as detailed in the Privacy Policy.
While Users may use the Springer Nature journal content for small scale, personal non-commercial use, it is important to note that Users may not:

1. use such content for the purpose of providing other users with access on a regular or large scale basis or as a means to circumvent access control;
2. use such content where to do so would be considered a criminal or statutory offence in any jurisdiction, or gives rise to civil liability, or is otherwise unlawful;
3. falsely or misleadingly imply or suggest endorsement, approval , sponsorship, or association unless explicitly agreed to by Springer Nature in writing;
4. use bots or other automated methods to access the content or redirect messages
5. override any security feature or exclusionary protocol; or
6. share the content in order to create substitute for Springer Nature products or services or a systematic database of Springer Nature journal content.

In line with the restriction against commercial use, Springer Nature does not permit the creation of a product or service that creates revenue, royalties, rent or income from our content or its inclusion as part of a paid for service or for other commercial gain. Springer Nature journal content cannot be used for inter-library loans and librarians may not upload Springer Nature journal content on a large scale into their, or any other, institutional repository.
These terms of use are reviewed regularly and may be amended at any time. Springer Nature is not obligated to publish any information or content on this website and may remove it or features or functionality at our sole discretion, at any time with or without notice. Springer Nature may revoke this licence to you at any time and remove access to any copies of the Springer Nature journal content which have been saved.
To the fullest extent permitted by law, Springer Nature makes no warranties, representations or guarantees to Users, either express or implied with respect to the Springer nature journal content and all parties disclaim and waive any implied warranties or warranties imposed by law, including merchantability or fitness for any particular purpose.
Please note that these rights do not automatically extend to content, data or other material published by Springer Nature that may be licensed from third parties.
If you would like to use or distribute our Springer Nature journal content to a wider audience or on a regular basis or in any other manner not expressly permitted by these Terms, please contact Springer Nature at

onlineservice@springernature.com